ADVANCED FUNCTIONAL MATERIALS
www.afm-journal.de

Electromechanics of Domain Walls in Uniaxial Ferroelectrics

*Haidong Lu, Yueze Tan, Leonie Richarz, Jiali He, Bo Wang, Dennis Meier, Long-Qing Chen, and Alexei Gruverman**

Piezoresponse force microscopy (PFM) is used for investigation of the electromechanical behavior of the head-to-head (H-H) and tail-to-tail (T-T) domain walls on the non-polar surfaces of three uniaxial ferroelectric materials with different crystal structures: $LiNbO_3$, $Pb_5Ge_3O_{11}$, and $ErMnO_3$. It is shown that, contrary to the common expectation that the domain walls should not exhibit any PFM response on the non-polar surface, an out-of-plane deformation of the crystal at the H-H and T-T domain walls occurs even in the absence of the out-of-plane polarization component due to a specific form of the piezoelectric tensor. In spite of their different symmetry, in all studied materials, the dominant contribution comes from the counteracting shear strains on both sides of the H-H and T-T domain walls. The finite element analysis approach that takes into account a contribution of all elements in the piezoelectric tensor, is applicable to any ferroelectric material and can be instrumental for getting a new insight into the coupling between the electromechanical and electronic properties of the charged ferroelectric domain walls.

1. Introduction

Piezoresponse force microscopy (PFM) is a surface characterization technique widely used in the ferroelectric research. It is based on the detection of the electromechanical sample oscillations induced via the converse piezoelectric effect by an ac field applied using a sharp probing tip in contact with the sample surface.[1–4] The PFM response is usually interpreted as a vertical displacement of the cantilever due to the sample extension/compression associated with the out-of-plane polarization (vertical PFM), or a twisting motion of the cantilever due to the shear strain resulting from the in-plane polarization (lateral PFM).[5] PFM allows precise control and manipulation of the ferroelectric domain walls (DWs) along with a deeper insight into their physical properties.[6,7] In particular, recent experiments on non-polar surfaces of ferroelectric materials—where the polarization P is fully in-plane—revealed intriguing electronic properties associated with the polarization discontinuity at charged head-to-head (H-H) and tail-to-tail (T-T) DWs.[8–10] In addition, spatial variations of the electric order and strain can occur in close proximity to these DWs, giving rise to unusual polarization configurations and topological phenomena.[11] Notably, deviation of polarization from the allowed crystallographic direction should result in an enhanced piezoelectric effect along the nonpolar direction, which, in principle, should be detectable by PFM. However, a complex form of the piezoelectric tensor by itself may introduce a strong orientation dependence of the piezoelectric strain at the DWs. In addition, elastic strain in the vicinity of DWs could make a significant impact on their electronic properties. Thus, comparative studies of the electromechanical behavior of nominally charged and electrically neutral DWs on non-polar surfaces are highly desirable to better understand the polarization alignment and strain distribution at different types of domain boundaries. In this regard, uniaxial ferroelectrics, where only two antiparallel polarization states can exist, represent an ideal model system for this kind of studies as they allow preparation of the well-defined nonpolar sample surfaces.

In this work, we investigate the electromechanical behavior of the DWs in three uniaxial ferroelectrics with different crystal structures: lead germanate $Pb_5Ge_3O_{11}$ (PGO), lithium niobate $LiNbO_3$ (LNO) and erbium manganite $ErMnO_3$ (EMO). PFM imaging of the nominally charged and electrically neutral DWs has been carried out on the non-polar surfaces of the crystals and their electromechanical responses have been simulated by finite element modeling (FEM) using their full piezoelectric matrices. Our results reveal that, in spite of different symmetry, in all of these materials, the H-H and T-T DWs exhibit a strong out-of-plane piezoresponse in striking contrast to the PFM response from the in-plane polarization domains delineated by these DWs. This finding is indicative of a general fact that the non-trivial electromechanics of the DWs on non-polar

H. Lu, A. Gruverman
Department of Physics and Astronomy
University of Nebraska
Lincoln, NE 68588, USA
E-mail: agruverman2@unl.edu
Y. Tan, B. Wang, L.-Q. Chen
Department of Materials Science and Engineering
Pennsylvania State University
University Park, PA 16802, USA
L. Richarz, J. He, D. Meier
Department of Materials Science and Engineering
Norwegian University of Science and Technology (NTNU)
7491 Trondheim, Norway
The ORCID identification number(s) for the author(s) of this article can be found under https://doi.org/10.1002/adfm.202213684.

© 2023 The Authors. Advanced Functional Materials published by Wiley-VCH GmbH. This is an open access article under the terms of the Creative Commons Attribution-NonCommercial-NoDerivs License, which permits use and distribution in any medium, provided the original work is properly cited, the use is non-commercial and no modifications or adaptations are made.

DOI: 10.1002/adfm.202213684

surfaces is mainly driven by local non-uniformity of the piezoelectric properties across the H-H and T-T DWs. This local non-uniformity is a sufficient condition for the out-of-plane strain at the H-H and T-T DWs, which does not necessarily require polarization deviation from the allowed crystallographic direction. Analysis of the electromechanical behavior based on the full piezoelectric tensor provides a general method for the interpretation of the PFM signals from the DWs, which is applicable to any ferroelectric material.

2. Results

The in-plane and out-of-plane electromechanical responses of the nominally charged and neutral DWs have been recorded on non-polar surfaces by means of lateral PFM (LPFM) and vertical PFM (VPFM), respectively, employed in the resonance enhanced mode (see Methods for details). Schematics of the PFM imaging geometry for the H-H, T-T, and neutral DWs are shown in Figure 1a,d,g. The PFM phase signal is calibrated following procedures in Ref. [12].

2.1. Lithium Niobate

LPFM and VPFM images of the H-H, T-T and neutral DWs in the *x*-cut LNO crystal ($P \parallel c$) are shown in **Figure 1**. In the LPFM images (Figure 1b,e,h), the DWs appear in a conventional way: they exhibit a low PFM amplitude signal in comparison to the antiparallel in-plane domains delineated by these walls. On the other hand, in the VPFM images, the DWs show an abnormally strong amplitude signal in comparison to that of the domains (Figure 1c,f,i). In addition, in VPFM, there is a 180° phase difference between the H-H and T-T walls. This means that the T-T DWs oscillate in-phase with the ac modulation bias (showing expansion upon positive bias), while the H-H DWs are out-of-phase (showing contraction upon positive bias). Interestingly, two parallel electrically neutral 180° DWs (marked as nw #1 and nw #2 in Figure 1h) separating antiparallel side-by-side domains, exhibit opposite phase contrast in VPFM, which stems from the specific asymmetry of the $+z/-z/+z$ domain configuration. Cross-sectional analysis of the profiles of the PFM amplitude signals across the studied DWs (Figure 1j–l) reveals that all walls exhibit a significant out-of-plane strain illustrated by a strong VPFM amplitude signal. Note that we ruled out possible non-piezoelectric parasitic sources of the observed signal (see Note S1, Supporting Information).[13–15]

2.2. Lead Germanate

To verify that the above observations are of general nature, the same experiments have been carried out using the *y*-cut PGO single crystals ($P \parallel c$), where nominally charged H-H, T-T, and neutral DWs are routinely present after crystal growth (**Figure 2**). The LPFM measurements yield results similar to the *x*-cut LNO (Figure 2a,c,e). The VPFM images of the H-H and

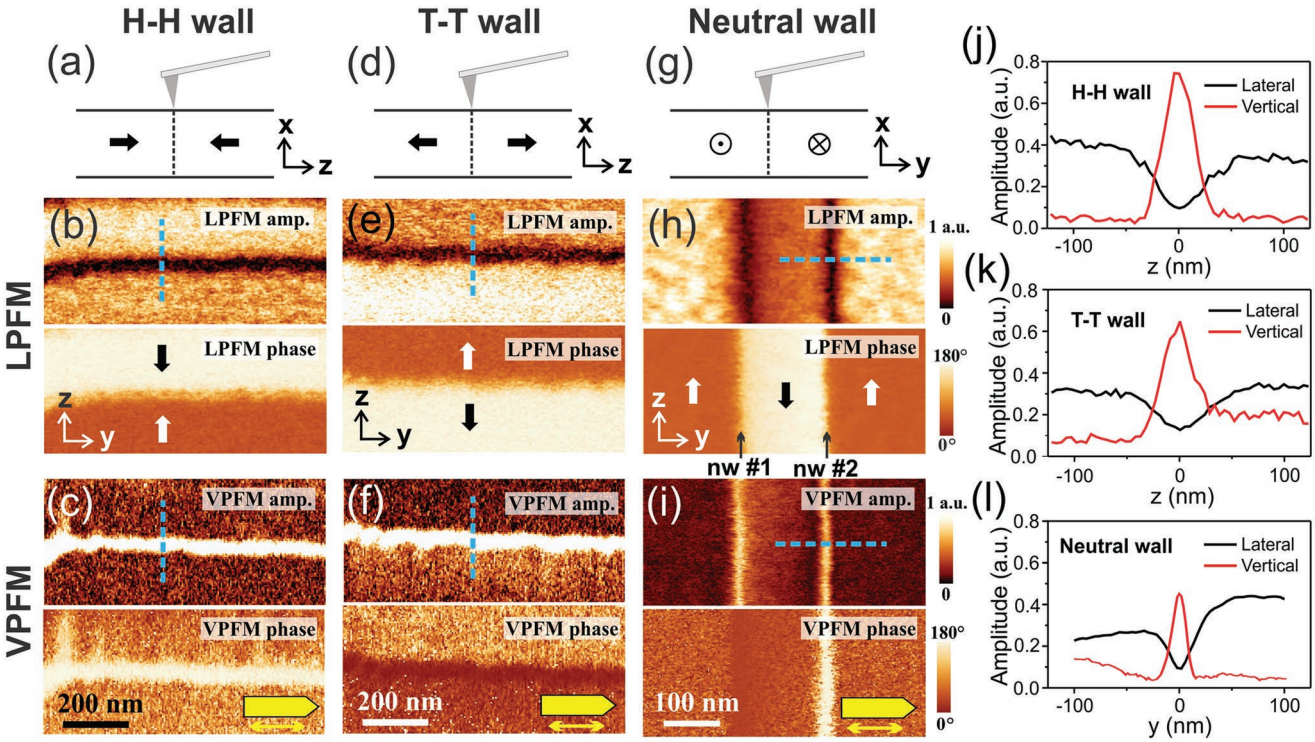

Figure 1. a–i) Experimental geometry and PFM images of the DWs on the non-polar surface of *x*-cut LNO: H-H (a–c), T-T (d–f), and neutral (g–i) DWs. Black and white arrows indicate the polarization directions in the adjacent domains. The cantilever orientation and a fast scanning direction are indicated in (c,f,i). j–l) Cross-sectional profile of the LPFM and VPFM amplitude signals across the H-H (j), T-T (k), and neutral (l) DWs along the dashed blue lines in (b–i).

© 2023 The Authors. Advanced Functional Materials published by Wiley-VCH GmbH

16163028, 2023, 15, Downloaded from https://onlinelibrary.wiley.com/doi/10.1002/adfm.202213684 by Norwegian Institute Of Public Healt Invoice Receipt DFO, Wiley Online Library on [14/01/2024]. See the Terms and Conditions (https://onlinelibrary.wiley.com/terms-and-conditions) on Wiley Online Library for rules of use; OA articles are governed by the applicable Creative Commons License

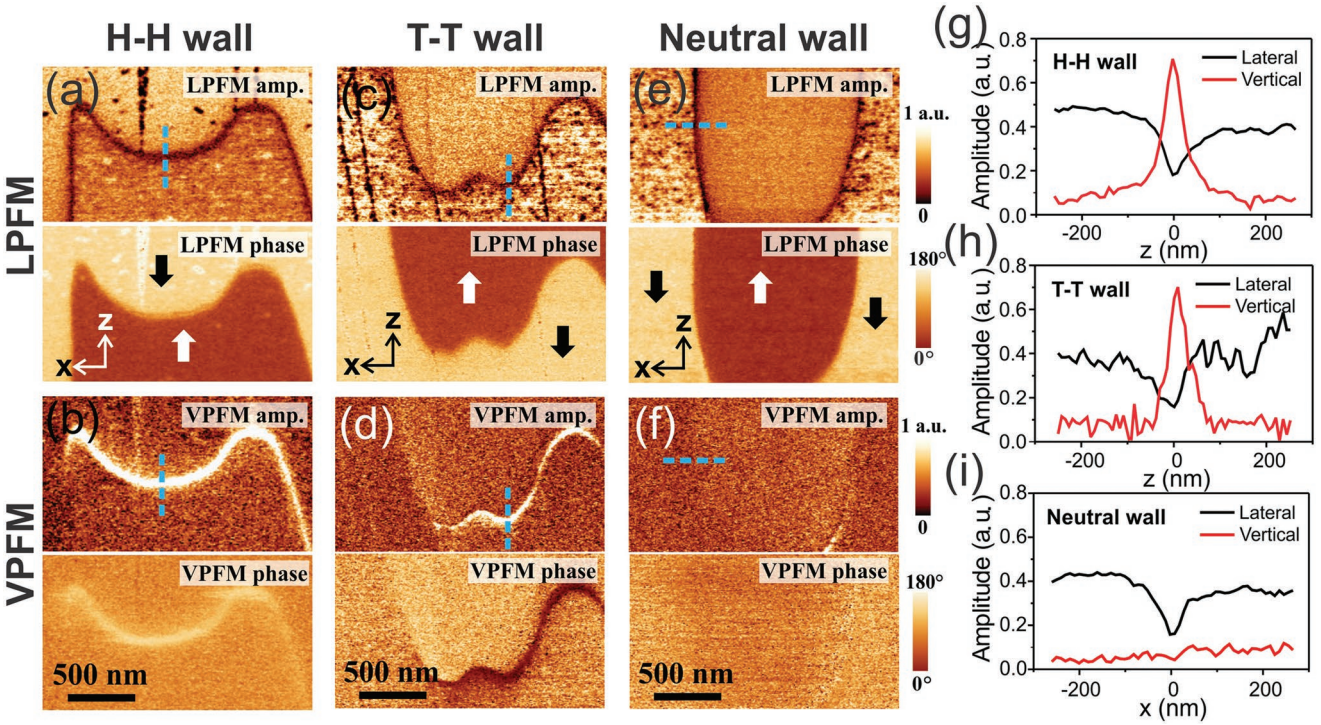

Figure 2. PFM images of the DWs on the nonpolar surface of *y*-cut PGO: H-H (a,b), T-T (c,d), and neutral (e,f) DWs. Black and white arrows indicate the polarization directions in the adjacent domains. g–i) Cross-sectional profile of the LPFM and VPFM amplitude signal across the H-H (g), T-T (h), and neutral (i) DWs along the dashed blue lines in (a–f).

T-T DWs acquired in PGO also appear to be similar to those observed in the *x*-cut LNO, i.e., these DWs exhibit strong amplitude signals and opposite phase signals (Figure 2b,d). However, no clear VPFM signal has been measured on the neutral 180° DWs in PGO (Figure 2f).

2.3. Erbium Manganite

Results of the VPFM imaging of an *x*-cut EMO crystal ($P \| c$) are shown in **Figure 3**. At first glance, the H-H and T-T DWs in this material exhibit a different electromechanical behavior: while the VPFM amplitude signal at the T-T DWs is stronger than the background signal, it is significantly weaker at the H-H DWs (Figure 3b,d). This effect can be attributed to the background signal (see cross-sectional profiles in Figure 3g–i), typically caused by the tip-sample potential mismatch.[16] An important point here is that the vertical piezoresponse signal from the H-H and T-T DWs is different from that of the domains. At the same time, no discernible VPFM signal (other than the uniform background signal) is detected at the neutral DWs (Figure 3f) similar to the case of PGO.

3. Modeling of the Domain Wall Electromechanical Response

To understand the origin of the observed out-of-plane strain at the DWs on the non-polar surfaces, we simulate their electromechanical response using the FEM following the work by Lei et al.[17] There, a quasistatic approach within a decoupled approximation framework was adopted. Specifically, the electrostatic potential distribution due to a biased tip located at a fixed point on the DW is first calculated. Then, the strain induced by converse piezoelectric effect is computed with the anisotropic piezoelectric tensors. Finally, the displacement field is obtained by solving the mechanical equilibrium equation. A hemispherical tip geometry is used in the calculation with a fixed tip-sample contact radius of 25 nm and a constant tip bias of +5 V. Details can be found in Experimental Section.

3.1. Lithium Niobate

LNO belongs to the point group 3*m* and its piezoelectric tensor contains four independent piezoelectric components: d_{15}, d_{22}, d_{31}, and d_{33} in Voigt notation. Details of the piezoelectric coefficient values are given in Experimental Section. **Figure 4** shows the modeling results of the electromechanical response of the DWs in the *x*-cut LNO sample. The calculated 2D out-of-plane displacement maps (Figure 4b,e) and the cross-sectional analysis of displacement (Figure 4c,f) reveal negative out-of-plane strain at the H-H DWs as well as at one of the neutral DWs (nw #2 in Figure 1h). The cross-section profiles across the DWs through the tip-sample contact also show sample contraction (Figure 4g,i) in agreement with the experimental data in Figure 1. The computed out-of-plane surface displacement maps for the T-T DW and for the other neutral DW (nw #1 in Figure 1h) are shown in Figure S2 (Supporting Information).

© 2023 The Authors. Advanced Functional Materials published by Wiley-VCH GmbH

16163028, 2023, 15, Downloaded from https://onlinelibrary.wiley.com/doi/10.1002/adfm.202213684 by Norwegian Institute Of Public Healt Invoice Receipt DFO, Wiley Online Library on [14/01/2024]. See the Terms and Conditions (https://onlinelibrary.wiley.com/terms-and-conditions) on Wiley Online Library for rules of use; OA articles are governed by the applicable Creative Commons License

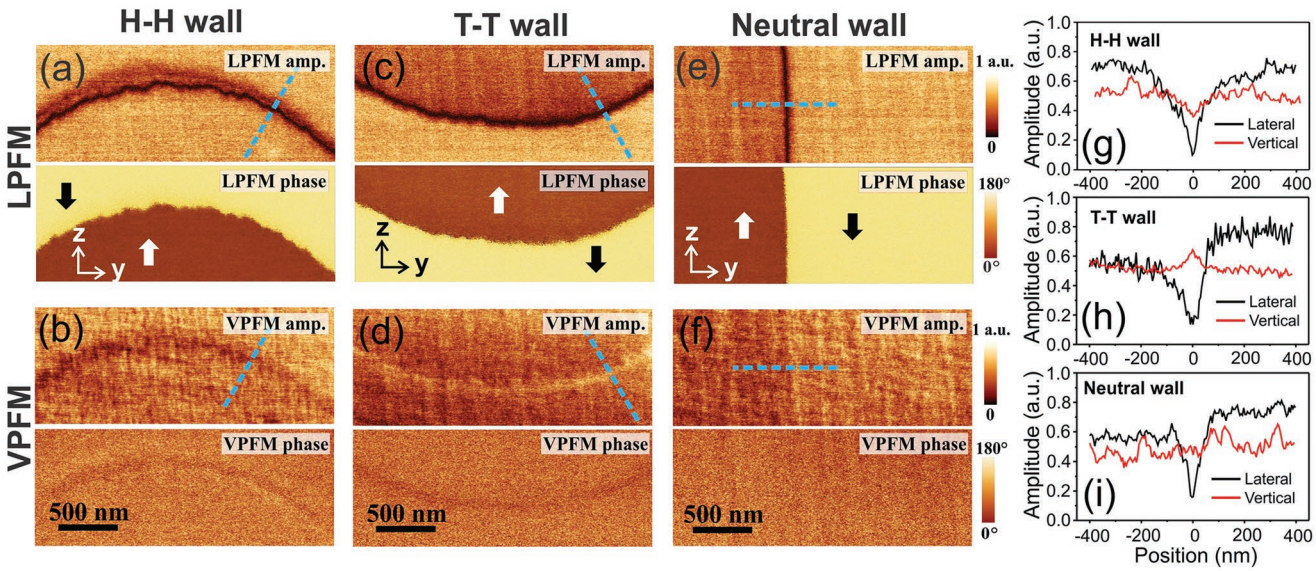

Figure 3. PFM images of the DWs on the non-polar surface of $ErMnO_3$: H-H (a,b), T-T (c,d), and neutral (e,f) DWs. Black and white arrows indicate the polarization directions in the adjacent domains. g–i) Cross-sectional profiles of the LPFM and VPFM amplitude signals across the H-H (g), T-T (h), and neutral (i) DWs along the dashed blue lines in (a–f). Note that there is a background signal in the VPFM mode.

To investigate the relative contribution of each piezoelectric coefficient to the VPFM signal, we use a modified piezoelectric tensor, which includes only specific piezoelectric coefficients related to the out-of-plane strain by symmetry (see Experimental Section for details). The calculated contributions of each independent piezoelectric component, i.e., d_{15}, d_{22}, d_{31}, and d_{33}, to the out-of-plane displacements at the H-H and neutral DWs are plotted in Figure 4 h,j as line profiles across the walls. It can be seen that the shear piezocoefficient, d_{15}, plays a dominant role in the out-of-plane strain at the H-H and T-T DWs in the *x*-cut LNO sample. Due to this coefficient, the out-of-plane component of the electric field (E_x) induces the piezoelectric shear strain ($d_{15}E_x$) in the *xz*-plane in the domains on both sides of the DW.[5] Since the dipole moments of these domains are

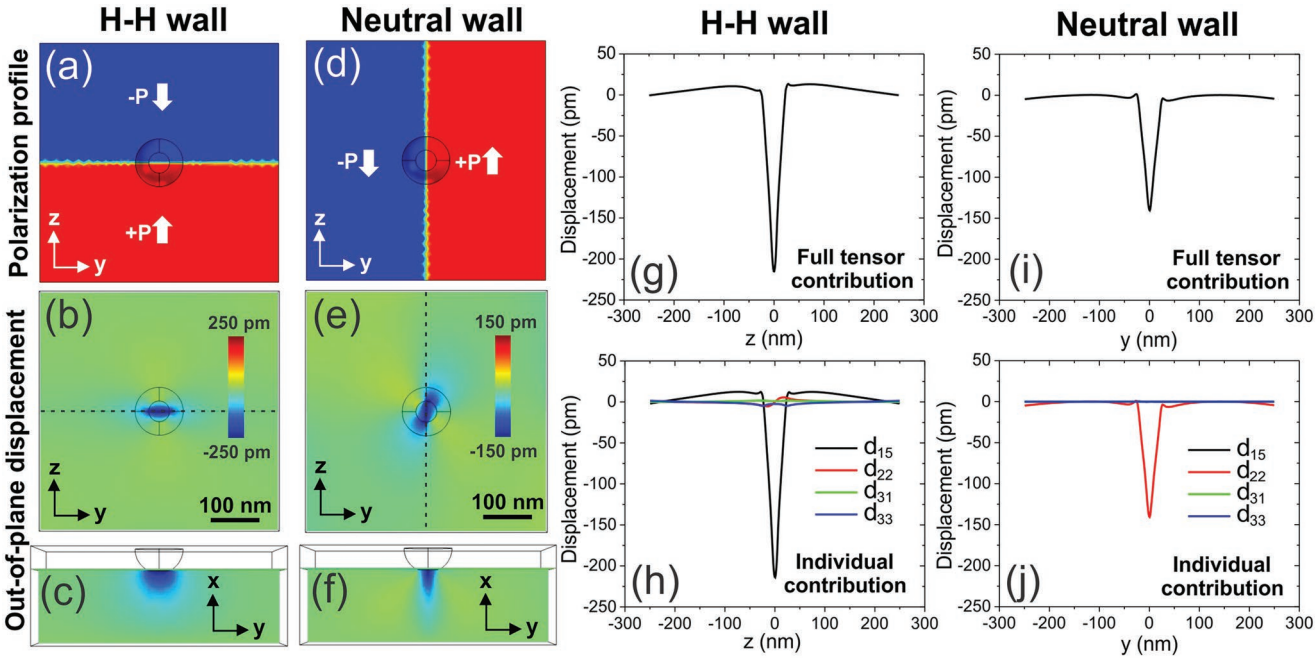

Figure 4. Modeling of the out-of-plane displacement of the of *x*-cut LNO surface (induced by a biased tip sitting at the domain wall). a–f) Polarization configuration (a,d) and the out-of-plane displacements observed on the *yz*-plane (b,e) and the cross-sectional *xy*-plane (c,f) for the H-H (a–c) and the neutral (d–f) DWs. The circles in (a–f) indicate the tip position. g–j) Cross-sectional profiles of the out-of-plane displacements across the DWs (along *z*-axis for the H-H (g,h) and *y*-axis for the neutral (i,j) DWs, respectively): due to the full piezoelectric tensor contribution (g,i) and the individual contributions from each piezoelectric coefficient (h,j).

© 2023 The Authors. Advanced Functional Materials published by Wiley-VCH GmbH

16163028, 2023, 15, Downloaded from https://onlinelibrary.wiley.com/doi/10.1002/adfm.202213684 by Norwegian Institute Of Public Healt Invoice Receipt DFO, Wiley Online Library on [14/01/2024]. See the Terms and Conditions (https://onlinelibrary.wiley.com/terms-and-conditions) on Wiley Online Library for rules of use; OA articles are governed by the applicable Creative Commons License

antiparallel, the shear strain flips its sign across the H-H and T-T DWs. This effectively results in a non-zero net out-of-plane strain and cancellation of the in-plane strain. Due to the mechanical compatibility conditions, unit cell volume conservation, shear strain in the antiparallel domains results in an upward surface displacement at the T-T DW forming a ridge, while the same mechanism leads to the downward surface displacement and formation of a valley at the H-H DW. In VPFM, this behavior will be manifested by a strong amplitude signal both for the H-H and T-T DWs and a 180° difference between their phase signals, consistent with the experimental data in Figure 1.

For the neutral 180° DWs, the d_{22} piezocoefficient is mainly responsible for the out-of-plane displacement through two contributions: i) a shear strain ($d_{16}E_x = -2d_{22}E_x$) in the *xy*-plane (normal to the neutral DW) with the opposite sign across the wall, and ii) an out-of-plane transverse strain ($d_{21}E_y = -d_{22}E_y$) that has the same sign across the wall since both the piezoelectric tensor and the tip-induced in-plane electric field, E_y, have opposite signs across the DW.

3.2. Lead germanate

PGO belongs to the point group 3 with the piezoelectric matrix containing six independent piezoelectric components: d_{11}, d_{14}, d_{15}, d_{22}, d_{31}, and d_{33} (see Section Methods for details). Similar to LNO and in agreement with the experimental data in Figure 2, the FEM modeling of the surface displacements at the DWs in the *y*-cut PGO reveals negative out-of-plane strain at the H-H DWs (**Figure 5**a,c) and positive out-of-plane strain at the T-T DWs (not shown). The out-of-plane displacement at the T-T and H-H DWs is due to shear strain deformation in the *yz*-plane dominated by d_{15} ($d_{24}E_y = d_{15}E_y$) (similar to the charged DWs in LNO). In addition, there is a contribution due to the out-of-plane transverse strain ($d_{32}E_z = d_{31}E_z$) that maintains its sign across the wall. Both these contributions lead to a downward out-of-plane displacement at the H-H wall (Fig. 5d) and upward out-of-plane displacement at the T-T wall (not shown).

In the vicinity of the neutral DWs, the calculations show a gradual transition from negative to positive strain across the DW with the strain being cancelled out right at the wall (Figure 5b,e) in agreement with the data in Figure 2. This behavior is due to the major contribution from the discontinuous out-of-plane longitudinal strain ($d_{22}E_y$), which yields an out-of-plane displacements of the opposite sign across the DW. It is likely that the gradual change of strain has not been picked up by VPFM because the actual tip-sample contact area is larger than was assumed for the calculations. The shear strain in the *xy*-plane ($d_{26}E_y = -2d_{11}E_y$) and the out-of-plane transverse strain ($d_{12}E_x = -d_{11}E_y$), which also may induce an out-of-plane

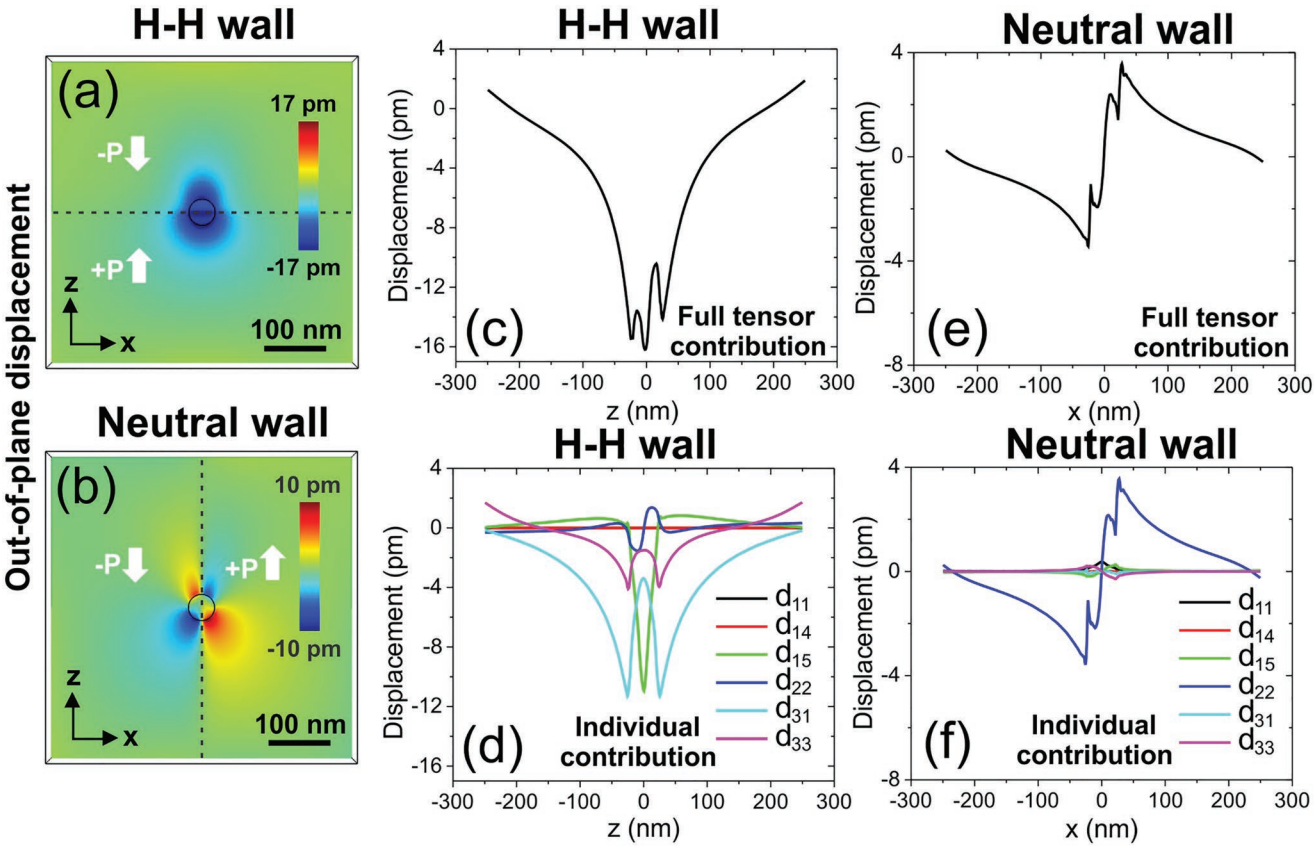

Figure 5. Modeling of the out-of-plane displacement of the *y*-cut PGO surface (induced by a biased tip sitting at the domain wall). a,b) The out-of-plane displacement observed on the *xz*-plane for the H-H (a) and the neutral (b) DWs. c–f) Cross-sectional profiles of the out-of-plane displacements across the DWs (along *z*-axis for the H-H (c,d) and *x*-axis for the neutral wall (e,f) DWs, respectively): due to the full piezoelectric tensor contribution (c,e) and the individual contributions from each piezoelectric coefficient (d,f).

© 2023 The Authors. Advanced Functional Materials published by Wiley-VCH GmbH

16163028, 2023, 15, Downloaded from https://onlinelibrary.wiley.com/doi/10.1002/adfm.202213684 by Norwegian Institute Of Public Healt Invoice Receipt DFO, Wiley Online Library on [14/01/2024]. See the Terms and Conditions (https://onlinelibrary.wiley.com/terms-and-conditions) on Wiley Online Library for rules of use; OA articles are governed by the applicable Creative Commons License

displacement, are negligibly small due to a small value of d_{11} (~0.1 pm/V).

3.3. Erbium manganite

The EMO crystals with point group symmetry 6*mm* are characterized by a piezoelectric tensor with the following independent piezoelectric coefficients: d_{15}, d_{31}, and d_{33} (see Experimental Section for details). In this crystal, the elastic and dielectric properties are identical along the *x*- and *y*-directions. Hence, the d_{15} component dominates the out-of-plane displacement of the charged DWs through the opposite shear strains ($d_{15}E_y$) on both sides of the H-H DWs (**Figure 6**a,b). Analogous results are obtained for T-T DWs (not shown). On the other hand, symmetry forbids any head-on shear strains and transverse strains of the same sign across the 180° neutral DWs, which results in zero net out-of-plane displacement at these walls (Figure 6c,d) in agreement with the data in Figure 3.

4. Discussion

The experimental results and FEM simulations demonstrate that symmetry breaking at the domain boundaries induce a piezoelectric response very different from that of the domains themselves, which represent regions with continuous symmetry. This implies that the VPFM signals observed at the domain boundaries on the nonpolar surfaces do *not* necessarily imply the existence of an out-of-plane polarization component within the DWs. Note that other interfaces, such as phase boundaries, also exhibit similar discontinuities, which may produce a profound electromechanical response. One particular example is an enhanced VPFM signal at the antiferroelectric-ferroelectric phase boundary in $CuInP_2Se_6$ reported by Dziaugys et al.[18] Thus, PFM measurements alone cannot provide conclusive evidence in support of the polarization deviation in the vicinity of the antiparallel domain junctions,[11] thereby necessitating additional high-resolution structural studies.

In general, depending on the material symmetry and the specific form of the piezoelectric tensor, out-of-plane strain at the DWs may be induced on the nonpolar surfaces either by the shear strain or by an out-of-plane transverse strain that retains its sign across the wall. In addition, as a secondary effect, head-on longitudinal strains ($d_{33}E_z$, for the charged DWs) across the DW may induce an out-of-plane displacement (similar to the Poisson effect). However, our modeling results suggest that this effect is typically an order of magnitude lower compared to the shear strain or out-of-plane transverse strain assuming the same order of magnitude of the piezoelectric coefficients.

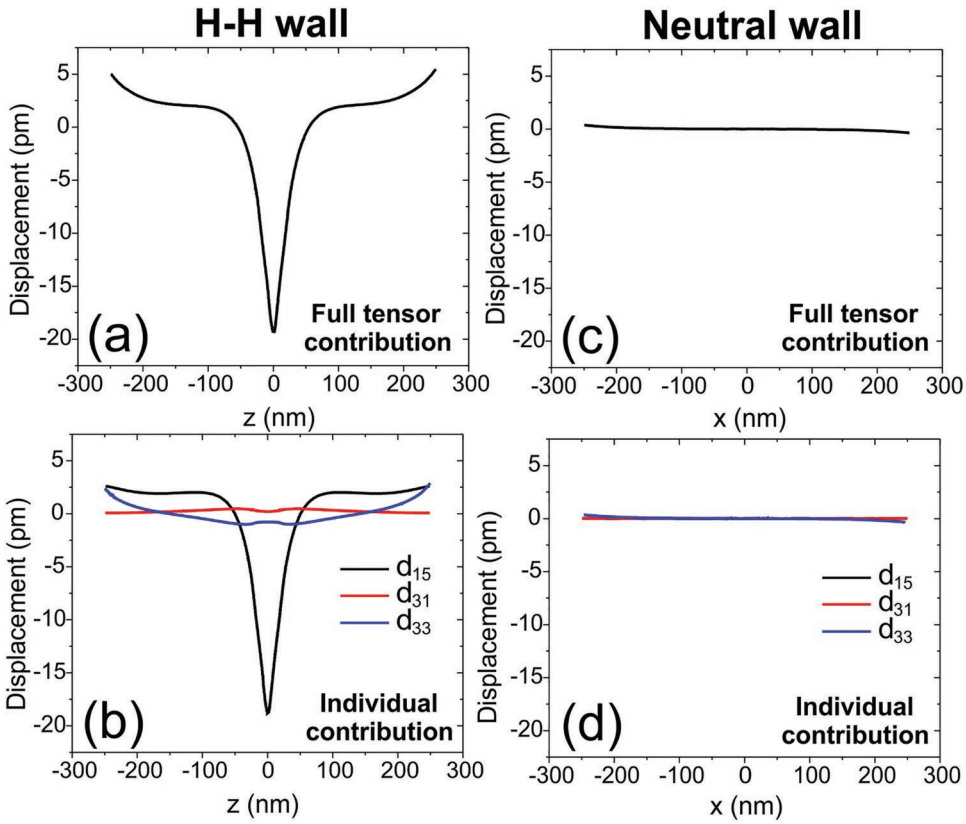

Figure 6. Modeling of the out-of-plane displacement on the *y*-cut EMO surface (induced by a biased tip sitting at the domain wall). a–d) Cross-sectional profiles of the out-of-plane displacements across the H-H (a,b) and the neutral (c,d) DWs due to the full piezoelectric tensor contribution (a,c) and the individual contributions from each piezoelectric coefficient (b,d).

© 2023 The Authors. Advanced Functional Materials published by Wiley-VCH GmbH

16163028, 2023, 15, Downloaded from https://onlinelibrary.wiley.com/doi/10.1002/adfm.202213684 by Norwegian Institute Of Public Healt Invoice Receipt DFO, Wiley Online Library on [14/01/2024]. See the Terms and Conditions (https://onlinelibrary.wiley.com/terms-and-conditions) on Wiley Online Library for rules of use; OA articles are governed by the applicable Creative Commons License

5. Conclusion

In conclusion, we have investigated the origin of the out-of-plane displacement at the ferroelectric H-H and T-T DWs on the nonpolar surfaces where the polarization P is fully in-plane. The obtained results show that symmetry breaking at the DWs plays the main role in producing a net out-of-plane strain at the H-H and T-T DWs. The dominant contribution comes from the counteracting shear strains on both sides of the H-H and T-T DWs. Notably, there is no difference between the electromechanical responses of the H-H and T-T DWs in PGO and LNO despite their completely different inner structure and different charge screening mechanisms. On the other hand, the electromechanical behavior of the neutral 180° DWs to a large extend depends on the specific material symmetry. The experimentally observed electromechanical behavior of the DWs has been simulated by finite element modeling that takes into account a contribution of all elements in the piezoelectric tensor. We emphasize that our analysis of the out-of-plane displacement of the nonpolar surface can be readily extended to ferroelectric materials with multiple polar axes although the situation could become more complicated in materials with ferroelastic DWs due to the additional elastic conditions. In general, it is important to analyze the specific electromechanical responses of these DWs in order to make correct attribution of the obtained PFM signal to the specific polarization state and electronic properties of the domain walls.

6. Experimental Section

Sample Preparation: Three hundred-nanometer-thick *x*-cut LNO single crystalline films on LNO substrates were prepared by the ion sliced method (NanoLN, Inc). PGO single crystals were grown by the Czochralski method and were cut along the (010) plane to obtain samples with nonpolar surfaces (*y*-cut). Mechanical polishing was used to achieve surfaces with optical quality. EMO single crystals were grown by the floating zone method.[19] The crystals were aligned by Laue diffraction and cut perpendicular to the hexagonal *c*-axis to achieve samples with in-plane polarization (*x*-cut). The surface was then chemomechanically polished with silica slurry.

Domain Writing in LNO: The H-H (T-T) walls on the x-cut LNO non-polar surface were prepared by moving a biased PFM tip at −70 V (+70 V) perpendicular to the polar direction, while the neutral walls were prepared by moving the biased tip along the polar direction.[20,21] PFM experiments were done 1 week after poling to allow dissipation of the injected charges during the poling process. As-grown domain walls were studied in the PGO and EMO crystals.[8,22]

PFM Imaging: PFM imaging was performed on commercial AFM systems (MFP-3D and Cypher, Asylum Research) using Pt-coated Si tips (PPP-EFM, Nanosensors) and Ti/Ir-coated Si tips (ASYLEEC.01-R2, Oxford Instruments). For reference, on the MFP-3D system, an ac modulation voltage of 0.8 V in amplitude with frequency around 650 kHz near torsional contact resonance was applied for LPFM imaging in the resonant enhanced PFM mode. For the PFM measurements on LNO and PGO, the ac modulation voltage of 0.8–1.5 V in amplitude with frequency ≈350 kHz near deflecting contact resonance was used. The PFM phase signal was calibrated following procedures in Ref. [12], i.e., 0° denoted an in-phase signal, and 180° indicated a signal, which is out-of-phase with the ac driving voltage.

Finite Element Modeling: The finite element modeling (FEM) simulation was performed in a block with a dimension of $500 \times 500 \times 150$ nm^3, where a DW normal (H-H or T-T wall) or parallel (neutral wall) to the polar axis separates the area into two regions with opposite polarization. Simulation of the electric field distribution was carried for a biased tip at +5 V DC assuming a circular tip-sample contact area of 25 nm in radius. The strain components induced by converse piezoelectricity are computed by $\varepsilon^0_{jk} = d_{ijk}\ E_i$ with the anisotropic piezoelectric tesnors in different domains. The displacement fields u_i and total strain components $\varepsilon_{ij} = (\nabla_i u_j + \nabla_j u_i)/2$ are solved from the elastic equilibrium equation $\nabla_j C_{ijkl}\ (\varepsilon_{kl} - \varepsilon^0_{kl}) = \nabla_j\ \nabla_k C_{ijkl} u_l - \nabla_j C_{ijkl}\ \varepsilon^0_{kl} = 0$ to ensure the mechanical compatibility.

In LNO, which belongs to the point group 3*m*, the piezoelectric matrix contains four independent components, i.e., d_{15}, d_{22}, d_{31}, and d_{33}, with the following values: d_{15} = 69.2 pm V^{-1}, d_{22} = 20.8 pm V^{-1}, d_{31} = −0.85 pm V^{-1}, and d_{33} = 6.0 pm V^{-1}.[23,24] The piezoelectric tensor in Voigt notation is given by

$$\begin{bmatrix} 0 & 0 & 0 & 0 & d_{15} & -2d_{22} \\ -d_{22} & d_{22} & 0 & d_{15} & 0 & 0 \\ d_{31} & d_{31} & d_{33} & 0 & 0 & 0 \end{bmatrix} \tag{1}$$

PGO belongs to the point group 3, where the piezoelectric matrix contains six independent piezoelectric components: d_{11}, d_{14}, d_{15}, d_{22}, d_{31}, and d_{33}, with values of d_{11} = 0.1 pm V^{-1}, d_{14} = 0.2 pm V^{-1}, d_{15} = 3.0 pm V^{-1}, d_{22} = 2.0 pm V^{-1}, d_{31} = 5.2 pm V^{-1}, and d_{33} = 6.2 pm V^{-1} ,[25] and the piezoelectric tensor is given by

$$\begin{bmatrix} d_{11} & -d_{11} & 0 & d_{14} & d_{15} & -d_{22} \\ -d_{22} & d_{22} & 0 & d_{15} & -d_{14} & -d_{11} \\ d_{31} & d_{31} & d_{33} & 0 & 0 & 0 \end{bmatrix} \tag{2}$$

In EMO, which belongs to the point group 6 *mm*, the piezoelectric matrix contains three independent components: d_{15}, d_{31}, and d_{33}. Here, values of d_{15} = 3.726 pm V^{-1}, d_{31} = −0.292 pm V^{-1}, and d_{33} = 0.804 pm V^{-1} found from the first-principles calculations were used. The piezoelectric tensor is given by

$$\begin{bmatrix} 0 & 0 & 0 & 0 & d_{15} & 0 \\ 0 & 0 & 0 & d_{15} & 0 & 0 \\ d_{31} & d_{31} & d_{33} & 0 & 0 & 0 \end{bmatrix} \tag{3}$$

The elastic stiffness tensors for LNO and PGO can be found in Refs. [23] and [25], respectively. The elastic stiffness tensor and background dielectric permittivity obtained from the DFT calculations are listed as below:

$$C_{\mathrm{EMO}} = \begin{bmatrix} 241.2 & 133.7 & 129.6 & & & \\ 133.7 & 241.2 & 129.6 & & & \\ 129.6 & 129.6 & 342.4 & & & \\ & & & 101.8 & & \\ & & & & 101.8 & \\ & & & & & 53.7 \end{bmatrix} \mathrm{GPa} \tag{4}$$

$$\varepsilon^{\mathrm{r}}_{\mathrm{EMO}} = \begin{bmatrix} 21.693 & & \\ & 21.723 & \\ & & 12.407 \end{bmatrix} \tag{5}$$

For the contribution of each piezoelectric coefficient to the out-of-plane displacement, the dielectric matrix and the elastic tensors were

© 2023 The Authors. Advanced Functional Materials published by Wiley-VCH GmbH

16163028, 2023, 15, Downloaded from https://onlinelibrary.wiley.com/doi/10.1002/adfm.202213684 by Norwegian Institute Of Public Healt Invoice Receipt DFO, Wiley Online Library on [14/01/2024]. See the Terms and Conditions (https://onlinelibrary.wiley.com/terms-and-conditions) on Wiley Online Library for rules of use; OA articles are governed by the applicable Creative Commons License

kept the same, while modifying the piezoelectric tensor to include only the specific piezoelectric coefficient and those related to it by symmetry and eliminate the rest. For example, to calculate the relative contribution of d_{11} in the case of PGO, the piezoelectric tensor was modified to

$$\begin{bmatrix} d_{11} & -d_{11} & 0 & 0 & 0 & 0 \\ 0 & 0 & 0 & 0 & 0 & -d_{11} \\ 0 & 0 & 0 & 0 & 0 & 0 \end{bmatrix} \tag{6}$$

Supporting Information

Supporting Information is available from the Wiley Online Library or from the author.

Acknowledgements

The authors would like to thank Edith Bourret and Zewu Yan for providing the EMO single crystals for this study. B.W. and L.Q.C. were supported by the National Science Foundation (NSF) through Grant No. DMR-1744213. Y.T. acknowledges the support from the National Science Foundation under grant DMR-2011839 through the MRSEC Center for Nanoscale Science of the Pennsylvania State University. The FEM simulations are performed by the Roar supercomputer of the Penn State Institute for Computational and Data Sciences.

Conflict of Interest

The authors declare no conflict of interest.

Data Availability Statement

The data that support the findings of this study are available from the corresponding author upon reasonable request.

Keywords

electromechanical responses, ferroelectric domain walls, piezoresponse force microscopy

Received: November 23, 2022
Revised: December 29, 2022
Published online: February 2, 2023

[1] A. Gruverman, S. V. Kalinin, *J. Mater. Sci.* **2006**, *41*, 107.
[2] S. V. Kalinin, D. A. Bonnell, *Phys. Rev. B* **2002**, *65*, 125408.
[3] N. Balke, I. Bdikin, S. V. Kalinin, A. L. Kholkin, *J Am Ceram Soc* **2009**, *92*, 1629.
[4] A. Gruverman, M. Alexe, D. Meier, *Nat. Commun.* **2019**, *10*, 1661.
[5] S. V. Kalinin, B. J. Rodriguez, S. Jesse, J. Shin, A. P. Baddorf, P. Gupta, H. Jain, D. B. Williams, A. Gruverman, *Microsc. Microanal.* **2006**, *12*, 206.
[6] G. Catalan, J. Seidel, R. Ramesh, J. F. Scott, *Rev. Mod. Phys.* **2012**, *84*, 119.
[7] D. Meier, S. M. Selbach, *Nat. Rev. Mater.* **2022**, *7*, 15.
[8] O. Bak, T. S. Holstad, Y. Tan, H. Lu, D. M. Evans, K. A. Hunnestad, B. Wang, J. P. V. McConville, P. Becker, L. Bohaty, I. Lukyanchuk, V. M. Vinokur, A. T. J. van Helvoort, J. M. Gregg, L.-Q. Chen, D. Meier, A. Gruverman, *Adv. Funct. Mater.* **2020**, *30*, 2000284.
[9] D. Meier, J. Seidel, A. Cano, K. Delaney, Y. Kumagai, M. Mostovoy, N. A. Spaldin, R. Ramesh, M. Fiebig, *Nat. Mater.* **2012**, *11*, 284.
[10] M. Schröder, A. Haußmann, A. Thiessen, E. Soergel, T. Woike, L. M. Eng, *Adv. Funct. Mater.* **2012**, *22*, 3936.
[11] Y. Tikhonov, J. R. Maguire, C. J. McCluskey, J. P. V. McConville, A. Kumar, H. Lu, D. Meier, A. Razumnaya, J. M. Gregg, A. Gruverman, V. M. Vinokur, I. Luk'yanchuk, *Adv. Mater.* **2022**, *34*, 2203028.
[12] P. Buragohain, H. Lu, C. Richter, T. Schenk, P. Kariuki, S. Glinsek, H. Funakubo, J. Íñiguez, E. Defay, U. Schroeder, A. Gruverman, *Adv. Mater.* **2022**, 2206237.
[13] S. Kim, D. Seol, X. Lu, M. Alexe, Y. Kim, *Sci. Rep.* **2017**, *7*, 41657.
[14] D. Seol, B. Kim, Y. Kim, *Curr. Appl. Phys.* **2017**, *17*, 661.
[15] L. Collins, Y. Liu, O. S. Ovchinnikova, R. Proksch, *ACS Nano* **2019**, *13*, 8055.
[16] T. Jungk, Á. Hoffmann, E. Soergel, *J Microsc* **2007**, *227*, 72.
[17] S. Lei, E. A. Eliseev, A. N. Morozovska, R. C. Haislmaier, T. T. A. Lummen, W. Cao, S. V. Kalinin, V. Gopalan, *Phys. Rev. B* **2012**, *86*, 134115.
[18] A. Dziaugys, K. Kelley, J. A. Brehm, L. Tao, A. Puretzky, T. Feng, A. O'Hara, S. Neumayer, M. Chyasnavichyus, E. A. Eliseev, J. Banys, Y. Vysochanskii, F. Ye, B. C. Chakoumakos, M. A. Susner, M. A. McGuire, S. V. Kalinin, P. Ganesh, N. Balke, S. T. Pantelides, A. N. Morozovska, P. Maksymovych, *Nat. Commun.* **2020**, *11*, 3623.
[19] Z. Yan, D. Meier, J. Schaab, R. Ramesh, E. Samulon, E. Bourret, *J. Cryst. Growth* **2015**, *409*, 75.
[20] A. V. Ievlev, D. O. Alikin, A. N. Morozovska, O. V. Varenyk, E. A. Eliseev, A. L. Kholkin, V. Y. Shur, S. V. Kalinin, *ACS Nano* **2015**, *9*, 769.
[21] H. Lu, T. Li, S. Poddar, O. Goit, A. Lipatov, A. Sinitskii, S. Ducharme, A. Gruverman, *Adv. Mater.* **2015**, *27*, 7832.
[22] D. Meier, J. Seidel, A. Cano, K. Delaney, Y. Kumagai, M. Mostovoy, N. A. Spaldin, R. Ramesh, M. Fiebig, *Nat. Mater.* **2012**, *11*, 284.
[23] R. T. Smith, F. S. Welsh, *J. Appl. Phys.* **1971**, *42*, 2219.
[24] M. Jazbinšek, M. Zgonik, *Appl. Phys. B* **2002**, *74*, 407.
[25] T. Yamada, H. Iwasaki, N. Niizeki, *J. Appl. Phys.* **1972**, *43*, 771.

© 2023 The Authors. Advanced Functional Materials published by Wiley-VCH GmbH

16163028, 2023, 15, Downloaded from https://onlinelibrary.wiley.com/doi/10.1002/adfm.202213684 by Norwegian Institute Of Public Healt Invoice Receipt DFO, Wiley Online Library on [14/01/2024]. See the Terms and Conditions (https://onlinelibrary.wiley.com/terms-and-conditions) on Wiley Online Library for rules of use; OA articles are governed by the applicable Creative Commons License